

The kinematics of multiple Compton scattering of two-photon systems

Peter Caradonna*

School of Physics, Engineering and Technology, The University of York, YO10 5DD, York, United Kingdom

(Dated: March 29, 2024)

We present a Stokes-Mueller method to calculate the cross sections associated with multiple Compton scattering of an arbitrary two-photon system. This method is used to calculate the cross section in the scenario in which one of the maximally entangled annihilation photons undergoes intermediate Compton scattering followed by the detection of both photons using a pair of Compton polarimeters. The method accounts for potential quantum-decoherence effects caused by Compton scattering. Despite being grounded in quantum field theory, the method does not require an in-depth understanding of its typically intricate prerequisites. As a result, this method is anticipated to be accessible to a broader community of physicists and is readily applicable in Monte Carlo simulations.

I. INTRODUCTION

A theoretical understanding of the decoherence effects arising from the interaction between entangled photonic systems and their environment is of fundamental importance. At the optical scale, understanding decoherence is crucial for fundamental tests and numerous quantum applications [1, 2]. At the MeV scale, where completely different interaction processes are relevant, there is currently no theoretical framework.

The joint differential Compton cross section for entangled annihilation photons (0.511 MeV) has long been solved within the framework of quantum field theory, for the case when each photon undergoes a scattering event [3, 4]. The cross section has not only provided a foundational understanding of the phenomenon of entanglement in Compton interactions, but has also provided the first theoretical prediction of entanglement witness in physics [5]. Nevertheless, a key challenge in this context is to establish a theoretical framework capable of calculating cross sections that account for decoherence effects when annihilation photons interact with their environment. This work presents the first such calculation, obtained for the decoherence of the entanglement in polarization between the photons via the dominant interaction process, viz. Compton scattering.

Annihilation photons play a crucial role in various fields, including fundamental physics [6, 7], material science [7, 8], and medical imaging such as Positron Emission Tomography (PET) [9, 10]. In such applications, the decoherence of the annihilation photons is an important but currently not understood phenomenon. For example, in typical PET imaging protocols [11] the measured events are dominated by those where intermediate Compton scattering of one or more annihilation photons has taken place before detection [12, 13]. This background scatter decreases the visibility of cancer growths in PET imaging [14–16]. The correct treatment of the leading (potentially decoherent) process of an intermediate scattering event is imperative for a wide range of applications,

not only PET, but also for any application or fundamental test where entangled photons are used. In addition to the medium through which the photons pass, we remark that typical photon detection systems at the MeV scale (e.g. scintillation crystals) will naturally have contributions from multiple Compton scattering. Therefore, due to the lack of any decoherence theory, correct modeling of the event topology in coincident detection of entangled photons is also currently lacking.

The most immediate application of a decoherence model is in recently proposed quantum-entangled PET (QE-PET). This introduces a novel paradigm in which Compton polarimeters replace the scintillation detectors found in conventional PET systems (or the standard segmented detector arrays are adapted for polarimetry through new analysis methods). Compton polarimeters belong to a category of position-sensitive devices capable of determining the orientation of the scattering plane of a Compton scattered photon [17]. Consequently, when operating in coincidence mode, a pair of Compton polarimeters can detect entanglement-induced correlations by analyzing the coincidence count rate of the scattered annihilation photons as a function of the relative angle between the scattering planes [18]. This technological shift is geared towards improving image quality by investigating and leveraging the quantum correlations that arise from the entanglement in the polarization between the annihilation photons [19–22].

The absence of a framework that accounts for the decoherence in n -Compton scattering ($n > 2$) has persisted for many decades, impeding the advancement of quantum technologies at the MeV energy scale such as QE-PET. Experimental constraints on 3-Compton scattering, specifically when one of the annihilation photons undergoes an intermediate Compton scattering event, have only been achieved in recent years [19, 23, 24]. Major programs of measures with improved statistics and kinematic coverage are already planned (JPET) [25]. The lack of any calculation of the entangled 3-Compton cross section led to the current approximation of the complete-entanglement loss in such events [19, 23].

We present the first calculation of the 3-Compton cross section for annihilation photons. This calculation is accomplished through a formalism that embeds the intrin-

* peter.caradonna@york.ac.uk

sic quantum field theory within a matrix representation for both the photon and the interacting Compton electron [26–28].

The novel formalism is adaptable to implementation in Monte Carlo simulations and exhibits flexibility in accommodating various reaction processes. As a result, this framework can be extended to include reaction processes occurring across a spectrum of photon energy scales. From a fundamental perspective, a 3-Compton scattering theory would provide the opportunity to test the predictions of quantum mechanics in more intricate scenarios.

II. THE DENSITY MATRIX OF THE COMPTON ELECTRONS

Wightman [26] introduced a novel matrix calculus that simplified the calculations of the cross sections related to double Compton scattering and those related to quantum correlations between entangled annihilation photons. These maximally entangled photons are formed when a positron and an electron with opposite spins annihilate each other. The Wightman approach encodes the underlying quantum field theory calculations in a form amenable to modeling a two-photon entangled system.

Wightman represented the Klein-Nishina cross section in the form of a 4×4 matrix that is averaged over the initial spin states and summed over the final spin states of the electron. Fano [27] later extended the applicability of the Compton matrix to include scattering off spin-polarized electrons.

McMaster [28] illustrated the extensive utility of the Fano Compton matrix and other Mueller matrices in calculating the cross sections of various polarized radiation and particles involved in different polarization-sensitive interactions. This method is shown to align with both quantum field theory calculations and experimental findings [29–32].

Schmidt and Simons identified a mathematical link between the Fano density matrix method and the McMaster method, further streamlining the calculation of cross sections for annihilation photons scattering off spin-polarized electrons [33]. Their calculations demonstrated agreement with the experimental data, which shows that their methodology produces results consistent with experimental observations.

Yet, the matrix method devised by the mentioned authors has not been expanded to compute cross sections for the multiple Compton scattering of an entangled two-photon systems. Consequently, understanding the effects of entanglement on the scattering results of these photon systems remains an open question, especially in the context of annihilation photons [19].

The goal of this section is to outline a method for obtaining a density matrix that characterizes the electrons involved in the multiple scattering of a beam of photons. This scattering is caused by a finite number of independent Compton electrons that can be in a spin-polarized

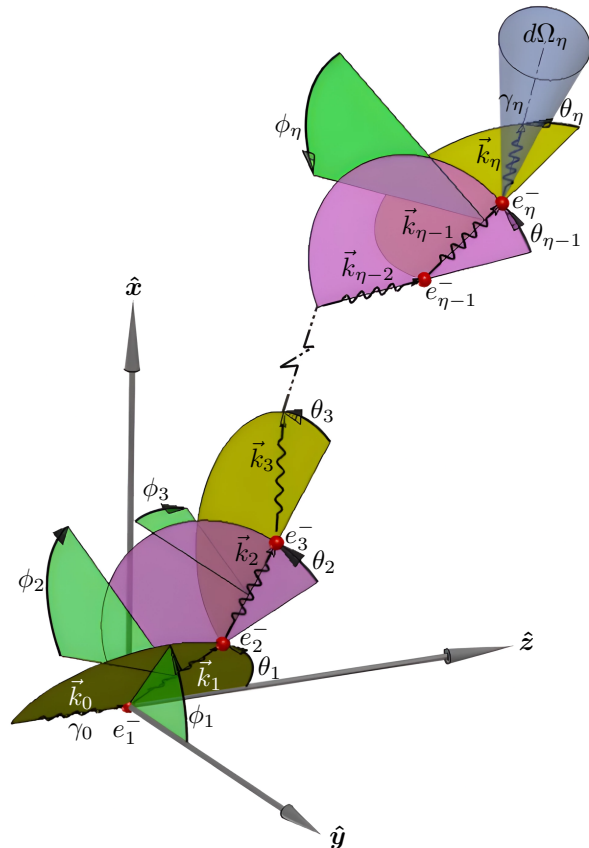


FIG. 1: An arbitrary polarized beam consisting of photons labeled γ_0 represented by the Stokes vector $|S\rangle$ undergoing η consecutive Compton scattering events by stationary independent electrons that can be in some state of polarization, see Appendix A for more detail. The azimuthal angle ϕ_j , when $j = 1$ (ϕ_1) is the angle between the scattering plane that contains the momentum vectors (\vec{k}_0, \vec{k}_1) and the $y - z$ plane. The azimuthal angle ϕ_j , where $1 < j \leq \eta$, is the angle between the scattering plane containing $(\vec{k}_{j-2}, \vec{k}_{j-1})$ and the scattering plane containing $(\vec{k}_{j-1}, \vec{k}_j)$. Polar angle θ_j , when $j = 1$ (θ_1) is the angle between z -axis and \vec{k}_1 . For $1 < j \leq \eta$, θ_j is the angle between \vec{k}_{j-1} and \vec{k}_j .

state configuration, as described in [27, 28]. Although the method is based on the specific scenario in which all of the struck electrons are initially at rest, the theory can encompass a broader range of situations, including those in which some or all of the electrons have non-zero momenta. This extension is achieved through the application of Lorentz transforms.

Let $\rho^{(1,2,\dots,\eta)}$ denote the density matrix that characterizes the distribution of η independent Compton electrons. In the Stokes-Mueller formalism, $\rho^{(1,2,\dots,\eta)}$ is defined in terms of Stokes parameters which are label here

as $S_a^{(1,2,\dots,\eta)}$ ($a = 0, 1, 2, 3$), such that

$$\rho^{(1,2,\dots,\eta)} = \frac{1}{2} \times \begin{bmatrix} S_0^{(1,2,\dots,\eta)} + S_3^{(1,2,\dots,\eta)} & S_1^{(1,2,\dots,\eta)} - iS_2^{(1,2,\dots,\eta)} \\ S_1^{(1,2,\dots,\eta)} + iS_2^{(1,2,\dots,\eta)} & S_0^{(1,2,\dots,\eta)} - S_3^{(1,2,\dots,\eta)} \end{bmatrix}. \quad (1)$$

In Section II A, a pair of $\rho^{(1,2,\dots,\eta)}$ will be used to describe the electrons involved in the Compton scattering of a two-photon system.

Consider a scenario in which a photon beam is initially in an arbitrary polarized state $|\varphi\rangle$ and each photon is labeled γ_0 . This state is expanded using the basis vectors $|0\rangle$ and $|1\rangle$, such that

$$|\varphi\rangle = c_1 |0\rangle + c_2 |1\rangle, \quad (2)$$

where the probability amplitudes c_1 and c_2 belong to the complex number field and satisfy the normalisation condition $|c_1|^2 + |c_2|^2 = 1$. The basis vectors $|0\rangle$ and $|1\rangle$ correspond to the right $|R\rangle$ and left $|L\rangle$ circularly polarized basis vectors, respectively, such that

$$|0\rangle := |R\rangle = \begin{bmatrix} 1 \\ 0 \end{bmatrix}, \quad |1\rangle := |L\rangle = \begin{bmatrix} 0 \\ 1 \end{bmatrix}.$$

The basis vectors $|0\rangle$ and $|1\rangle$ are eigenstates of the σ_3 Pauli matrix with eigenvalues of ± 1 unit of spin angular momentum, respectively, where

$$\sigma_3 = \begin{bmatrix} 1 & 0 \\ 0 & -1 \end{bmatrix}, \quad (3)$$

and where the projection of the spin is along the trajectory of state $|\varphi\rangle$.

The density matrix $|\varphi\rangle\langle\varphi|$ of state $|\varphi\rangle$ is given by

$$|\varphi\rangle\langle\varphi| = \begin{bmatrix} |c_1|^2 & c_1^* c_2 \\ c_1 c_2^* & |c_2|^2 \end{bmatrix}. \quad (4)$$

To derive the solutions for the Stokes parameters $S_a^{(1,2,\dots,\eta)}$, of the interacting electrons, it is necessary to re-express the density matrix $|\varphi\rangle\langle\varphi|$, of Eq.(4), in terms of its associated Stokes parameters that we label S_a .

Stokes parameters S_a are defined as the expectation values of the 2×2 unit matrix denoted by σ_0 and the Pauli spin matrices $\{\sigma_1, \sigma_2, \sigma_3\}$. These Stokes parameters are conveniently grouped together in the form of a four-vector represented using the bra-ket notation as $|S\rangle$, such that

$$|S\rangle = \begin{bmatrix} S_0 \\ S_1 \\ S_2 \\ S_3 \end{bmatrix} = \begin{bmatrix} \langle\varphi|\sigma_0|\varphi\rangle \\ \langle\varphi|\sigma_1|\varphi\rangle \\ \langle\varphi|\sigma_2|\varphi\rangle \\ \langle\varphi|\sigma_3|\varphi\rangle \end{bmatrix} = \begin{bmatrix} |c_1|^2 + |c_2|^2 \\ c_1 c_2^* + c_2 c_1^* \\ i(c_1 c_2^* - c_2 c_1^*) \\ c_1 c_1^* - c_2 c_2^* \end{bmatrix}, \quad (5)$$

where

$$\sigma_0 = \begin{bmatrix} 1 & 0 \\ 0 & 1 \end{bmatrix}, \quad \sigma_1 = \begin{bmatrix} 0 & 1 \\ 1 & 0 \end{bmatrix}, \quad \sigma_2 = \begin{bmatrix} 0 & -i \\ i & 0 \end{bmatrix},$$

and σ_3 is given in Eq.(3).

The set of four Stokes parameters represents physically measurable properties and completely characterizes the photon beam. Each component describes the fraction of intensity passing normally through a differential element of area in a direction confined to a differential solid angle element $d\Omega$ per unit of time. From the definition of the expectation values, one sees that $S_0 = 1$ is the total normalized intensity.

For a randomly polarized beam, the Stokes vector reduces to $S_0 = 1$ and $S_1 = S_2 = S_3 = 0$. The second parameter, S_1 , is the difference between the degree of linear polarization in the direction parallel and perpendicular to a specified reference plane. The third, S_2 , is the difference between the degree of linear polarization in directions $+45^\circ$ and -45° , and the fourth, S_3 , is the difference in the degree of circular polarization of the right and left.

By utilizing the definition of the Stokes parameters S_a , as given in Eq.(5), it can be shown that Eq.(4) is equivalently expressed as

$$|\varphi\rangle\langle\varphi| = \frac{1}{2} \begin{bmatrix} S_0 + S_3 & S_1 - iS_2 \\ S_1 + iS_2 & S_0 - S_3 \end{bmatrix}. \quad (6)$$

Let $|S_\eta\rangle$ represent the Stokes vector associated with the final photon, denoted as γ_η , following a total of η Compton scattering events, as shown in Fig. 1. McMaster [28] demonstrated that in the case of multiple Compton scattering, the matrices that transform $|S\rangle \mapsto |S_\eta\rangle$ are of the following type:

$$\begin{aligned} |S_\eta\rangle &= T_\eta M_\eta T_{\eta-1} M_{\eta-1} \cdots T_2 M_2 T_1 M_1 |S\rangle \\ &= \prod_{j=\eta}^1 T_j M_j |S\rangle. \end{aligned} \quad (7)$$

Here j is a descending integer of the product operator Π , such that j runs from $j = \eta, \eta - 1, \eta - 2, \dots, 1$. The definitions of the 4×4 Compton transition matrix T_j and the rotation matrix M_j can be found in Appendix A.

The differential cross section for detecting γ_η , as illustrated in Fig. 1, using a polarization filter characterized by a Stokes vector $|D_p\rangle$ (refer to Appendix B for more details and examples), is given by

$$\begin{aligned} \frac{d\sigma}{d\Omega_\eta} &= \frac{1}{2} \langle D_p | S_\eta \rangle \\ &= \frac{1}{2} \langle D_p | \prod_{j=\eta}^1 T_j M_j | S \rangle, \end{aligned} \quad (8)$$

where the differential unit of solid angle $d\Omega_\eta$ is defined by the area it covers on the surface of a sphere centered at

the point where the electron labeled e_{η}^{-} is located. The cross section given in Eq.(8) has already incorporated the necessary summing over the final electron spins.

However, at MeV energies, direct measurement of polarization faces experimental challenges due to the unavailability of polarization filters, unlike in the optical regime, where there is an abundant array of filters to choose from. Using a polarization-insensitive detector, we effectively measure each of the two orthogonal states of polarization and sum the results.

Let $|I\rangle$ denote the Stokes vector for a polarization-insensitive detector, where $|I\rangle = [1, 0, 0, 0]^T$ (refer to Appendix B for more details). In this case, the formula for the differential cross section becomes

$$\begin{aligned} \frac{d\sigma}{d\Omega_{\eta}} &= \langle I | S_{\eta} \rangle \\ &= \langle I | \prod_{j=\eta}^1 T_j M_j | S \rangle. \end{aligned} \quad (9)$$

If the Stokes vector $|S\rangle$ and the total number of Compton scattering events η are known, then the right-hand side of Eq.(8) or Eq.(9) can, in principle, be computed to determine the differential cross section.

However, the goal is to evaluate the right-hand side of Eq.(8) or Eq.(9) by expanding in terms of the Stokes parameters S_a . The coefficients of S_a will be used to construct the density matrix $\rho^{(1,2,\dots,\eta)}$, given in Eq.(1).

To accomplish this, we use the trace method approach of Schmidt and Simons [33], to calculate the differential cross section presented in Eq.(8) or Eq.(9) in a distinct but equivalent manner. Using $|\varphi\rangle\langle\varphi|$ given in Eq.(6) and $\rho^{(1,2,\dots,\eta)}$ from Eq.(1), the differential cross section can also be obtained by solving the expression:

$$\frac{d\sigma}{d\Omega_{\eta}} = \text{Tr} \left[|\varphi\rangle\langle\varphi| \cdot \rho^{(1,2,\dots,\eta)} \right]. \quad (10)$$

Evaluating the right hand side yields

$$\frac{d\sigma}{d\Omega_{\eta}} = \frac{1}{2} \sum_{a=0}^3 S_a S_a^{(1,2,\dots,\eta)}. \quad (11)$$

Now, equating the right hand side of Eq.(11) with the corresponding expression in Eq.(8), for a polarization filter characterized by a Stokes vector $|D_p\rangle$, leads to

$$\sum_{a=0}^3 S_{ia} S_a^{(1,2,\dots,\eta)} = \langle D_p | \prod_{j=\eta}^1 T_j M_j | S \rangle. \quad (12a)$$

Similarly, when equating the right hand side of Eq.(11) with that in Eq.(9), for a polarization-insensitive detector characterized by a Stokes vector $|I\rangle$, leads to

$$\sum_{a=0}^3 S_a S_a^{(1,2,\dots,\eta)} = 2 \langle I | \prod_{j=\eta}^1 T_j M_j | S \rangle. \quad (12b)$$

By expanding both the left and right sides of equations (12a) and (12b) with respect to S_a , we equate the coefficients corresponding to each S_a on both sides. Subsequently, these coefficients are solved in terms of $S_a^{(1,2,\dots,\eta)}$ which are expressed in relation to the known matrix elements associated with the matrices T_j and M_j . This process enables the determination of the density matrix given in Eq.(1), which characterizes the distribution of η independent Compton electrons. In Section III, we leverage Eq.(12b) to compute the 3-Compton differential cross section for annihilation photons.

A. Multiple Compton scattering of a general two-photon system

Consider some hypothetical device that emits a two-photon system defined by the density matrix ρ such that

$$\rho = \sum_{s=1}^N p_s |\psi_s\rangle\langle\psi_s|, \quad (13a)$$

where $\{|\psi_s\rangle\}_{s=1}^N$ represents a set of N ensemble 2-photon pure states. These states are not necessarily orthogonal, and each state is given by

$$\begin{aligned} |\psi_s\rangle &= c_{s1} \begin{bmatrix} 1 \\ 0 \\ 0 \\ 0 \end{bmatrix} + c_{s2} \begin{bmatrix} 0 \\ 1 \\ 0 \\ 0 \end{bmatrix} + c_{s3} \begin{bmatrix} 0 \\ 0 \\ 1 \\ 0 \end{bmatrix} + c_{s4} \begin{bmatrix} 0 \\ 0 \\ 0 \\ 1 \end{bmatrix} \\ &= c_{s1} |0, 0\rangle + c_{s2} |0, 1\rangle + c_{s3} |1, 0\rangle + c_{s4} |1, 1\rangle. \end{aligned} \quad (13b)$$

Alternatively, in terms of $|R\rangle$ and $|L\rangle$ notation, we can express $|\psi_s\rangle$ as

$$|\psi_s\rangle = c_{s1} |R, R\rangle + c_{s2} |R, L\rangle + c_{s3} |L, R\rangle + c_{s4} |L, L\rangle, \quad (13c)$$

where the probability amplitudes c_{sr} ($r = 1, 2, 3, 4$) satisfy the normalization condition

$$\sum_{r=1}^4 |c_{sr}|^2 = 1. \quad (13d)$$

The N number of weights labeled p_s satisfy the following conditions:

$$\sum_{s=1}^N p_s = 1; \quad 0 \leq p_s \leq 1. \quad (13e)$$

The normalization of the weights p_s ensures that $\text{Tr}[\rho] = 1$.

Figure (2) portrays a scenario where a pair of incident photons characterized by ρ and denoted as γ_{10} and γ_{20} each undergo multiple Compton scattering events. Specifically, γ_{10} Compton scatters from m electrons through a region designated as channel A, while γ_{20}

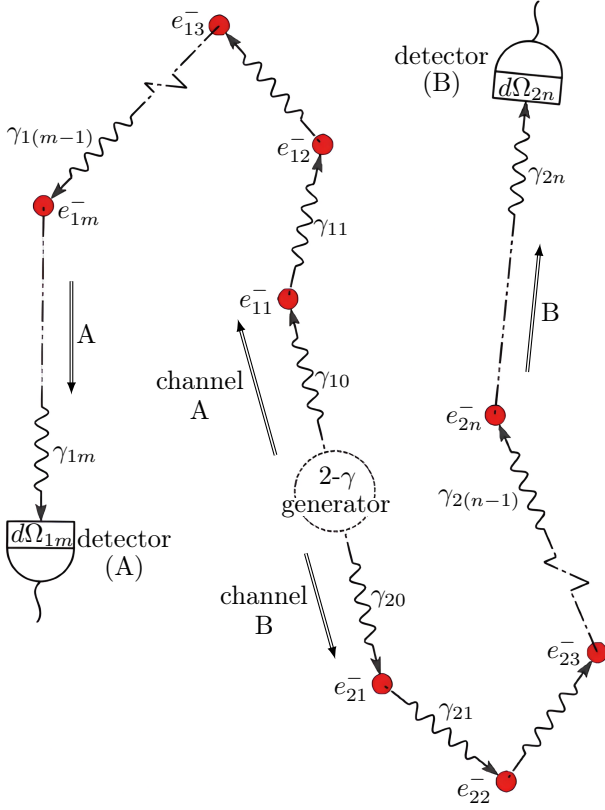


FIG. 2: A schematic illustrates multiple Compton scattering events involving a pair of incident photons, designated as γ_{10} and γ_{20} , of an arbitrary two-photon system. The photon γ_{10} undergoes m Compton scattering events through channel A, for which the m electrons are defined by the density matrix $\rho_A^{(1,2,\dots,m)}$. Similarly, the photon γ_{20} undergoes n Compton scattering events through channel B for which the n electrons are defined by the density matrix $\rho_B^{(1,2,\dots,n)}$. Subsequently, the photons exit channels A and B as γ_{1m} and γ_{2n} , respectively, before being analyzed using two space-like separated detectors that can be characterized by either the Stokes vector $|D_p\rangle$ or $|I\rangle$. (Refer to Appendix B for more information.)

Compton scatters from n electrons through a region designated as channel B. Here, m and n are positive integers, where $m + n$ represents the total number of scattering events by state ρ . The resulting electrons after the scattering events m and n are labeled γ_{1m} and γ_{2n} , respectively. Let $\rho_A^{(1,2,\dots,m)}$ and $\rho_B^{(1,2,\dots,n)}$ denote the density matrix of the m and n electrons of channel A and B,

respectively, where

$$\rho_A^{(1,2,\dots,m)} = \frac{1}{2} \times \begin{bmatrix} S_{10}^{(1,2,\dots,m)} + S_{13}^{(1,2,\dots,m)} & S_{11}^{(1,2,\dots,m)} - iS_{12}^{(1,2,\dots,m)} \\ S_{11}^{(1,2,\dots,m)} + iS_{12}^{(1,2,\dots,m)} & S_{10}^{(1,2,\dots,m)} - S_{13}^{(1,2,\dots,m)} \end{bmatrix}, \quad (14a)$$

and

$$\rho_B^{(1,2,\dots,n)} = \frac{1}{2} \times \begin{bmatrix} S_{20}^{(1,2,\dots,n)} + S_{23}^{(1,2,\dots,n)} & S_{21}^{(1,2,\dots,n)} - iS_{22}^{(1,2,\dots,n)} \\ S_{21}^{(1,2,\dots,n)} + iS_{22}^{(1,2,\dots,n)} & S_{20}^{(1,2,\dots,n)} - S_{23}^{(1,2,\dots,n)} \end{bmatrix}. \quad (14b)$$

If we now consider channels A and B to be space-like separated, the density matrix for the interacting electrons is given by the direct product

$$\rho_A^{(1,2,\dots,m)} \otimes \rho_B^{(1,2,\dots,n)}. \quad (15)$$

Using the trace operator, the joint differential scattering cross section of the two-photon system described by ρ is then given by

$$\frac{d^2\sigma}{d\Omega_{1m}d\Omega_{2n}} = \frac{1}{4} \text{Tr} \left[\rho \cdot \rho_A^{(1,2,\dots,m)} \otimes \rho_B^{(1,2,\dots,n)} \right], \quad (16)$$

where the differential unit of solid angle $d\Omega_{1m}$ and $d\Omega_{2n}$ are defined by the elemental area they cover on the surface of a sphere centered at the point where the electrons e_{1m}^- and e_{2n}^- , respectively, are located. By employing Eq.(12a) or Eq.(12b), one can derive the Stokes parameters $S_{1a}^{(1,2,\dots,m)}$ and $S_{2a}^{(1,2,\dots,n)}$. Consequently, the joint differential cross section, as provided in Eq.(16), can be computed with respect to the types of polarization analyzers intended to measure γ_{1m} and γ_{2n} .

III. 3-COMPTON CROSS SECTION

This section outlines the derivation of the 3-Compton cross section for annihilation photons. As in the previous theoretical work for 1- and 2-Compton scattering [3–5, 21, 28] the calculation is done for a free stationary electron. We remark that the electron binding energy and Fermi motion effects for 1-, 2- (and now 3-) Compton are taken into account when the theory is implemented in simulation [34]

Hence, we can employ the general formalism from the previous section to calculate the cross section for intermediate Compton scattering by one of the annihilation photons. This calculation refers to the use of two hypothetical Compton polarimeters in a 3-Compton scattering scenario: one scattering event that occurs inside the patient and one in each of the polarimeters labeled A and B, as illustrated in Fig. 3.

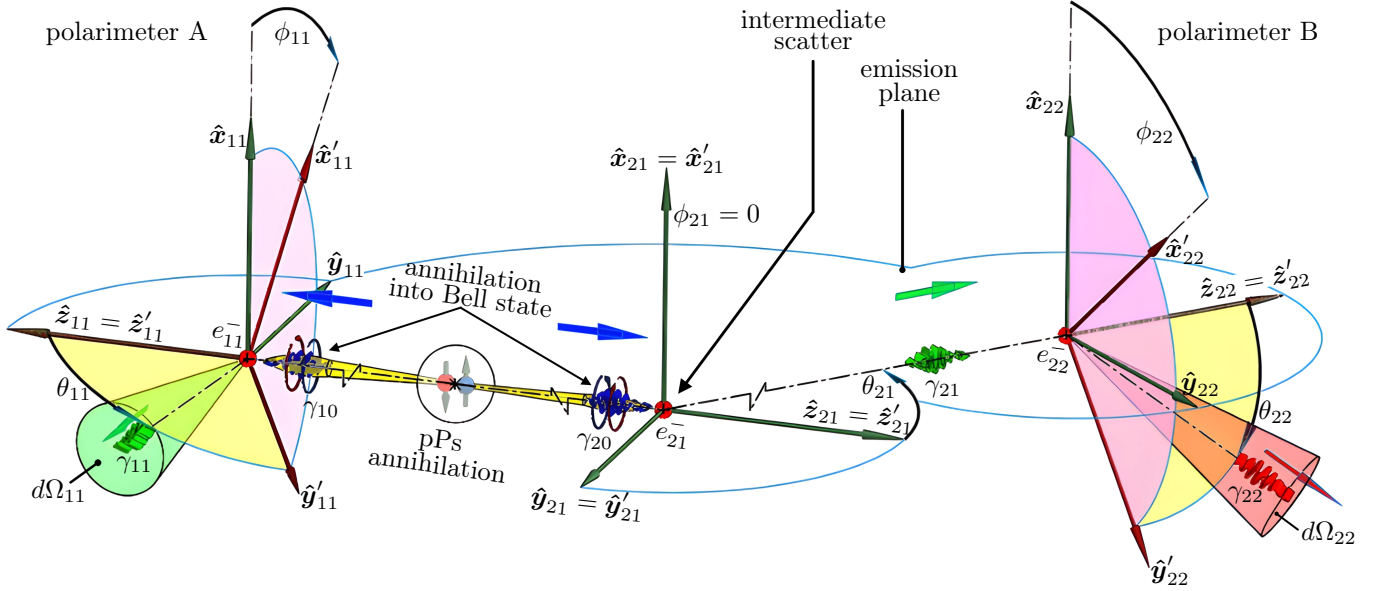


FIG. 3: The nomenclature for the annihilation of pPs emitting two 0.511 MeV photons, γ_{10} and γ_{20} , in a Bell state. Initially, the photons travel in opposite directions along the unit vectors \hat{z}_{11} and \hat{z}_{21} ($\hat{z}_{11} = -\hat{z}_{21}$). Three local coordinate systems are defined; $\{\hat{x}_{ij}, \hat{y}_{ij}, \hat{z}_{ij}\}$, where $i = 1, 2$ (labels photon 1 or 2) and $j = 1, 2$ (labels the coordinate system with an electron e_{ij} located at the origin). The coordinate systems are relative to an emission plane that contains the unit vectors $\{\hat{y}_{11}, \hat{z}_{11}\}$, $\{\hat{y}_{21}, \hat{z}_{21}\}$ and $\{\hat{y}_{22}, \hat{z}_{22}\}$. Compton events occur at the origin of each coordinate system. The intermediate scattering angle θ_{21} in the coordinate system $ij = 21$ is defined by $\hat{z}_{21} \cdot \hat{z}_{22} = \cos \theta_{21}$. The photon labeled γ_{21} is the photon that results from intermediate scattering. The relative angle between the scattering planes of γ_{11} and γ_{22} is determined by the dot product $\hat{x}'_{11} \cdot \hat{x}'_{22}$ (see Eq. (38)). We define two hypothetical Compton polarimeters, A and B, with respect to the coordinate systems with subscripts $ij = 11$ and $ij = 22$.

Using Eq.(13b), we set $s = 1$ and label the annihilation photons as γ_{10} and γ_{20} . These photons are assumed to be produced from the disintegration of parapositronium pPs in the ground state. The state $|\psi_1\rangle$ is in a Bell state described by

$$|\psi_1\rangle = \frac{1}{\sqrt{2}} |0, 0\rangle - \frac{1}{\sqrt{2}} |1, 1\rangle, \quad (17)$$

where $c_{11} = 1/\sqrt{2}$, $c_{14} = -1/\sqrt{2}$, and $c_{12} = c_{13} = 0$.

Using Eq.(13a), the 4×4 density matrix ρ describing state $|\psi_1\rangle$ takes the explicit form

$$\rho = |\psi_1\rangle \langle \psi_1| = \frac{1}{2} \begin{bmatrix} 1 & 0 & 0 & -1 \\ 0 & 0 & 0 & 0 \\ 0 & 0 & 0 & 0 \\ -1 & 0 & 0 & 1 \end{bmatrix}, \quad (18)$$

where $p_1 = 1$ and $p_s = 0$ for $s > 1$.

Due to the inherent symmetries in the state $|\psi_1\rangle$ [5], we are free to designate the intermediate Compton scattering event to γ_{20} without loss of generality. This implies that γ_{20} undergoes a double Compton scattering event.

Referring to Eq.(16), the joint differential scattering

cross section we wish to solve is given by

$$\frac{d^2\sigma}{d\Omega_{11}d\Omega_{22}} = \frac{1}{4} \text{Tr} \left[\rho \cdot \left(\rho_A^{(1)} \otimes \rho_B^{(1,2)} \right) \right]. \quad (19)$$

To simulate the PET environment, we will compute the cross section for the standard scenario where Compton scattering takes place from unpolarized electron spins. Note that when calculating cross sections for unpolarized electrons, a relatively simpler approach is available to obtain the solution for Eq.(19). In this scenario, we only need to consider the upper-left 3×3 submatrix of the T_j and M_j matrices [28]. Furthermore, the Stokes parameters with subscript $a = 3$ do not contribute terms to the final cross section calculation and can thus be neglected.

Applying Eq.(14a), the density matrix $\rho_A^{(1)}$, which characterizes the unpolarized electron labeled e_{11}^- involved in the Compton scattering of γ_{10} is given by

$$\rho_A^{(1)} = \frac{1}{2} \begin{bmatrix} S_{10}^{(1)} & S_{11}^{(1)} - iS_{12}^{(1)} \\ S_{11}^{(1)} + iS_{12}^{(1)} & S_{10}^{(1)} \end{bmatrix}. \quad (20)$$

Here, the subscript 1 in the Stokes parameters $S_{1a}^{(1)}$ ($a = 0, 1, 2$) signifies the interaction of e_{11}^- with γ_{10} . The solutions for $S_{1a}^{(1)}$ are determined in the context of using

a detector insensitive to polarization, characterized by the Stokes vector $|I\rangle$. To derive the solutions of $S_{1a}^{(1)}$, we employ Eq.(12b) and solve for

$$\sum_{a=0}^2 S_a S_{1a}^{(1)} = 2 \langle I | T_{11} M_{11} | S \rangle, \quad (21)$$

where the subscripts ‘11’ in the T_{11} and M_{11} matrices refer to the interaction matrices of the electron labeled e_{11}^- . By expanding in terms of S_a and equating coefficients on both the left and right sides of Eq.(21), it can be shown that

$$\rho_A^{(1)} = \frac{1}{2} r_0^2 \left(\frac{E_{11}}{E_{10}} \right)^2 \begin{bmatrix} t_{11}^{(11)} & t_{12}^{(11)} e^{-2i\phi_{11}} \\ t_{12}^{(11)} e^{2i\phi_{11}} & t_{11}^{(11)} \end{bmatrix}, \quad (22)$$

where r_0 is the classical electron radius. Furthermore, the superscript ‘(11)’ of the matrix elements labeled $t_{mn}^{(11)}$ refers to the interaction terms associated with the electron e_{11}^- , and the subscripts ‘mn’ refer to the position of the matrix element in the T_{11} matrix. The functional form of the $t_{mn}^{(11)}$ matrix elements can be found in Appendix C.

The term E_{10} represents the incident kinetic energy of γ_{10} , and in natural units, $E_{10} = 1$ (0.511 MeV) for annihilation photons. The term E_{11} denotes the kinetic energy of γ_{11} , which is the result of the scattering of γ_{10} by e_{11}^- . The value of this term is calculated using the Compton relation formula given by

$$E_{11} = \frac{1}{2 - \cos \theta_{11}}; \quad (E_{10} = 1). \quad (23)$$

$$2 \langle I | T_{22} M_{22} T_{21} | S \rangle = \frac{r_0^4}{2} \left(\frac{E_{22}}{E_{20}} \right)^2 \begin{bmatrix} t_{11}^{(22)} & t_{12}^{(22)} & 0 \\ t_{12}^{(22)} & 2 - t_{12}^{(22)} & 0 \\ 0 & 0 & t_{33}^{(22)} \end{bmatrix} \begin{bmatrix} 1 & 0 & 0 \\ 0 & \cos 2\phi_{22} & \sin 2\phi_{22} \\ 0 & -\sin 2\phi_{22} & \cos 2\phi_{22} \end{bmatrix} \begin{bmatrix} t_{11}^{(21)} & t_{12}^{(21)} & 0 \\ t_{12}^{(21)} & 2 - t_{12}^{(21)} & 0 \\ 0 & 0 & t_{33}^{(21)} \end{bmatrix} \begin{bmatrix} S_0 \\ S_1 \\ S_2 \end{bmatrix}, \quad (26)$$

where the superscript ‘(21)’ and ‘(22)’ of the $t_{mn}^{(21)}$ and $t_{mn}^{(22)}$ matrix elements refer to the interaction terms associated with the electron e_{21}^- and e_{22}^- , respectively. The functional form of the matrix elements $t_{mn}^{(2r)}$ ($r = 1, 2$) is given in Appendix C.

The term E_{20} represents the incident kinetic energy of γ_{20} , and in natural units, $E_{20} = E_{10} = 1$ for the annihilation photons. The term E_{21} denotes the kinetic energy of γ_{21} , which is the result of the scattering of γ_{20} by e_{21}^- . This term is determined by the Compton relation formula given by

$$E_{21} = \frac{1}{2 - \cos \theta_{21}}; \quad (E_{20} = 1). \quad (27a)$$

Using Eq.(14b), the density matrix $\rho_B^{(1,2)}$, which characterizes the unpolarized electrons labeled e_{21}^- and e_{22}^- , is given by

$$\rho_B^{(1,2)} = \frac{1}{2} \begin{bmatrix} S_{20}^{(1,2)} & S_{21}^{(1,2)} - i S_{22}^{(1,2)} \\ S_{21}^{(1,2)} + i S_{22}^{(1,2)} & S_{20}^{(1,2)} \end{bmatrix}. \quad (24)$$

Here, the subscript 2 in the Stokes parameters $S_{2a}^{(1,2)}$ ($a = 0, 1, 2$) signifies the interaction of γ_{20} and γ_{21} with electrons e_{21}^- and e_{22}^- , respectively. The intermediate scattering of $\gamma_{20} \mapsto \gamma_{21}$ occurs at a polar angle of θ_{21} and an azimuthal angle of ϕ_{21} (set to 0 degrees), and in the case of an unpolarized electron, $S_{23}^{(1,2)} = 0$. Following this, the photon γ_{21} undergoes another Compton scatter, $\gamma_{21} \mapsto \gamma_{22}$, inside polarimeter B, with the direction of scatter defined by the polar angle θ_{22} and the azimuthal angle ϕ_{22} . (Refer to Fig. 3)

Applying Eq.(12b) gives the following expression for this case:

$$\sum_{a=0}^2 \left(S_a S_{2a}^{(1,2)} \right) = 2 \langle I | T_{22} M_{22} T_{21} M_{21} | S \rangle, \quad (25)$$

where the subscripts ‘21’ and ‘22’ in the $T_{21} M_{21}$ and $T_{22} M_{22}$ matrices refer to the interaction matrices of the electrons labeled e_{21}^- and e_{22}^- , respectively.

Since $\phi_{21} = 0$, M_{21} reduces to the 3×3 identity matrix (refer to Appendix A). As a result, the right-hand side of Eq.(25) takes on the explicit form:

The term E_{22} denotes the kinetic energy of γ_{22} , which is the result of the scattering of γ_{21} by e_{22}^- in polarimeter B and is given by

$$E_{22} = \frac{E_{21}}{1 + E_{21} (1 - \cos \theta_{22})}. \quad (27b)$$

After evaluating Eq.(26) with Eq.(25), which is ex-

panded in terms of S_a one can show that

$$\begin{aligned}
& S_{20}^{(1,2)} S_0 + S_{21}^{(1,2)} S_1 + S_{22}^{(1,2)} S_2 = \\
& \frac{r_0^4}{2} \left(\frac{E_{22}}{E_{20}} \right)^2 \left[\left(t_{11}^{(21)} t_{11}^{(22)} + t_{12}^{(21)} t_{12}^{(22)} \cos 2\phi_{22} \right) S_0 + \right. \\
& \quad \left(t_{12}^{(21)} t_{11}^{(22)} + \left(2 - t_{12}^{(21)} \right) t_{12}^{(22)} \cos 2\phi_{22} \right) S_1 + \\
& \quad \left. t_{33}^{(21)} t_{12}^{(22)} \sin 2\phi_{22} S_2 \right].
\end{aligned} \tag{28}$$

This implies that

$$S_{20}^{(1,2)} = \frac{r_0^4}{2} \left(\frac{E_{22}}{E_{20}} \right)^2 \left(t_{11}^{(21)} t_{11}^{(22)} + t_{12}^{(21)} t_{12}^{(22)} \cos 2\phi_{22} \right), \tag{29a}$$

$$\begin{aligned}
S_{21}^{(1,2)} &= \frac{r_0^4}{2} \left(\frac{E_{22}}{E_{20}} \right)^2 \times \\
&\quad \left(t_{12}^{(21)} t_{11}^{(22)} + \left(2 - t_{12}^{(21)} \right) t_{12}^{(22)} \cos 2\phi_{22} \right),
\end{aligned} \tag{29b}$$

$$\begin{aligned}
S_{22}^{(1,2)} &= \frac{r_0^4}{2} \left(\frac{E_{22}}{E_{20}} \right)^2 t_{33}^{(21)} t_{12}^{(22)} \sin 2\phi_{22} \\
&= \frac{r_0^4}{2} \left(\frac{E_{22}}{E_{20}} \right)^2 2 \sin \theta_{21} t_{12}^{(22)} \sin 2\phi_{22},
\end{aligned} \tag{29c}$$

where we have substituted the explicit form of $t_{33}^{(21)} = 2 \sin \theta_{21}$ in Eq.(29c) [27, 28].

By substituting the results obtained in Eq.(29) into Eq.(24), we determine the density matrix $\rho_B^{(1,2)}$. Using equations (18), (22) and (24), the joint differential cross section of Eq.(19) can be fully determined analytically and is given by

$$\frac{d^2\sigma}{d\Omega_{11}d\Omega_{22}} = \frac{r_0^6}{32} \left(\frac{E_{11}E_{22}}{E_0^2} \right)^2 P(\theta_{11}, \theta_{22}, \phi_{11}, \phi_{22}; \theta_{21}), \tag{30}$$

where we have set $E_{10} = E_{20} = E_0$. The function P can be expressed as

$$\begin{aligned}
P &= A(\theta_{11}, \theta_{22}; \theta_{21}) - B(\theta_{11}, \theta_{22}; \theta_{21}) C(\phi_{11}, \phi_{22}; \theta_{21}) + \\
&\quad D(\theta_{11}, \theta_{22}, \phi_{11}, \phi_{21}; \theta_{21}),
\end{aligned} \tag{31}$$

where

$$A(\theta_{11}, \theta_{22}; \theta_{21}) = t_{11}^{(11)} t_{11}^{(21)} t_{11}^{(22)}, \tag{32a}$$

$$B(\theta_{11}, \theta_{22}) = 2 t_{12}^{(11)} t_{12}^{(22)}, \tag{32b}$$

$$\begin{aligned}
C(\phi_{11}, \phi_{22}; \theta_{21}) &= \cos 2\phi_{11} \cos 2\phi_{22} - \\
&\quad \cos \theta_{21} \sin 2\phi_{11} \sin 2\phi_{22},
\end{aligned} \tag{32c}$$

and

$$\begin{aligned}
D(\theta_{11}, \theta_{22}, \phi_{11}, \phi_{22}; \theta_{21}) &= t_{12}^{(21)} \times \\
&\quad \left[t_{12}^{(22)} \cos 2\phi_{22} \left(t_{11}^{(11)} + t_{12}^{(11)} \cos 2\phi_{11} \right) - t_{12}^{(11)} t_{11}^{(22)} \cos 2\phi_{11} \right],
\end{aligned} \tag{32d}$$

such that the cross section is parameterized in terms of the intermediate polar angle θ_{21} . The matrix elements $t_{11}^{(pq)}$ represent the average differential cross section of scattering, regardless of polarization, and therefore the function $A(\theta_{11}, \theta_{22}; \theta_{21})$ represents the uncorrelated part of the 3-Compton scattering. On the other hand, the terms $t_{12}^{(pq)}$ indicate deviations from cylindrical symmetry in the scattered intensity [27].

IV. RESULTS

Referring to Eq.(30) and Appendix C, in the limit $\theta_{21} \mapsto 0$, we have $C \mapsto \cos 2(\phi_{11} + \phi_{22})$, $t_{12}^{(21)} \mapsto 0$, which implies that $D \mapsto 0$, $t_{11}^{(21)} \mapsto 2$, and $E_{21} \mapsto E_{20}$. In this situation, Eq. (30) reduces to

$$\begin{aligned}
&\left(\frac{r_0^2}{2} \right) \left(\frac{r_0^4}{16} \right) \left(\frac{E_{11}}{E_0} \right)^2 \left(\frac{E_{22}}{E_0} \right)^2 \times \\
&\quad \left[t_{11}^{(11)} t_{11}^{(22)} - t_{12}^{(11)} t_{12}^{(22)} \cos 2(\phi_{11} + \phi_{22}) \right], \quad \text{for } \theta_{21} = 0.
\end{aligned} \tag{33}$$

With the exception of a factor of $r_0^2/2$, this result precisely corresponds to the well-known Pryce-Ward cross section for 2-Compton scattering of annihilation photons [3].

To analyze the 3-Compton cross section given in Eq.(30) in the general case where the intermediate scattering angle $0 \leq \theta_{21} \leq \pi$, we simplify the analysis by setting $\theta_{11} = \theta_{22} = \theta$. This choice restricts the analysis to a subset of possible scattering geometries. With this condition, we can simplify the notation as follows: $A(\theta_{11}, \theta_{22}; \theta_{21}) \mapsto A(\theta; \theta_{21})$, $B(\theta_{11}, \theta_{22}) \mapsto B(\theta)$, and $D(\theta_{11}, \theta_{22}, \phi_{11}, \phi_{22}; \theta_{21}) \mapsto D(\theta, \phi_{11}, \phi_{22}; \theta_{21})$, while the function $C(\phi_{11}, \phi_{22}; \theta_{21})$ remains unchanged.

Furthermore, the forthcoming analysis will involve ratios of quantities. In these cases, factors other than the function P in Eq.(30) cancel out when ratios are taken. For this reason, only the function P given in Eq.(31) is considered.

We examine four scattering scenarios depicted in Fig. 4, each varying in the orientation of the scattering planes of γ_{11} and γ_{22} with respect to the emission plane.

In Fig. 4a, both the scattering planes of γ_{11} and γ_{22} lie within the emission plane ($\phi_{11} = \phi_{22} = 0$). Let $P^\parallel(\theta; \theta_{21})$ define this probability such that

$$\begin{aligned}
P^\parallel(\theta; \theta_{21}) &= \\
&\quad A(\theta; \theta_{21}) - B(\theta) C(0, 0; \theta_{21}) + D(\theta, 0, 0; \theta_{21}).
\end{aligned} \tag{34a}$$

In Fig. 4b, the scattering plane of γ_{11} is perpendicular

to the emission plane ($\phi_{11} = \pi/2$), while the scattering plane of γ_{22} is in the emission plane ($\phi_{22} = 0$). Let $P_{11}^{\perp}(\theta; \theta_{21})$ define this probability such that

$$P_{11}^{\perp}(\theta; \theta_{21}) = A(\theta; \theta_{21}) - B(\theta) C\left(\frac{\pi}{2}, 0; \theta_{21}\right) + D\left(\theta, \frac{\pi}{2}, 0; \theta_{21}\right). \quad (34b)$$

In Fig. 4c, the scattering plane of γ_{11} is parallel to the emission plane ($\phi_{11} = 0$), while the scattering plane of γ_{22} is perpendicular to the emission plane ($\phi_{22} = \pi/2$). Let $P_{22}^{\perp}(\theta; \theta_{21})$ define this probability such that

$$P_{22}^{\perp}(\theta; \theta_{21}) = A(\theta; \theta_{21}) - B(\theta) C\left(0, \frac{\pi}{2}; \theta_{21}\right) + D\left(\theta, 0, \frac{\pi}{2}; \theta_{21}\right). \quad (34c)$$

Finally, in Fig. 4d, the scattering plane of γ_{11} and γ_{22} are perpendicular to the emission plane ($\phi_{11} = \phi_{22} = \pi/2$). Let $P_{(11,22)}^{\perp}(\theta; \theta_{21})$ define this probability such that

$$P_{(11,22)}^{\perp}(\theta; \theta_{21}) = A(\theta; \theta_{21}) - B(\theta) C\left(\frac{\pi}{2}, \frac{\pi}{2}; \theta_{21}\right) + D\left(\theta, \frac{\pi}{2}, \frac{\pi}{2}; \theta_{21}\right). \quad (34d)$$

From the probabilities defined in Eq.(34), we calculate the following expected counting ratios, denoted as Z :

$$Z_{11}^{\perp} = \frac{P_{11}^{\perp}(\theta; \theta_{21})}{P^{\parallel}(\theta; \theta_{21})}, \quad Z_{22}^{\perp} = \frac{P_{22}^{\perp}(\theta; \theta_{21})}{P^{\parallel}(\theta; \theta_{21})}, \quad (35a)$$

and we define the average of the counting ratios given by Z_{av}^{\perp} such that

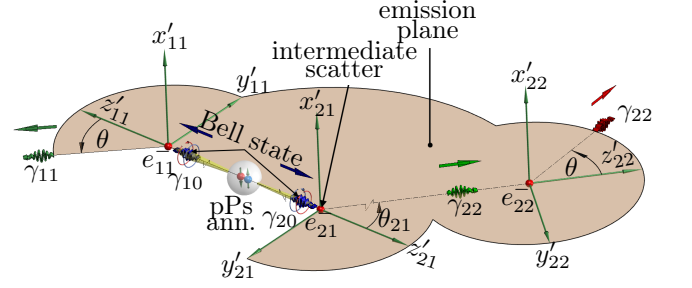
$$Z_{av}^{\perp} = \frac{1}{2} (Z_{11}^{\perp} + Z_{22}^{\perp}). \quad (35b)$$

Equations (35a) and (35b) represent the expected ratios for an ideal experiment using the scattering geometries shown in Fig. 4b and Fig. 4c, respectively, normalized by the counting rate defined by the scattering geometry shown in Fig. 4a. These ratios are plotted in Fig. 5 as a function of both θ and θ_{21} .

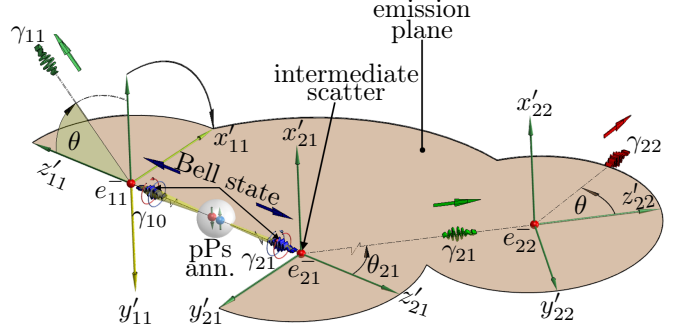
Furthermore, we define the ratio $Z_{(11,22)}^{\perp}$ as

$$Z_{(11,22)}^{\perp} = \frac{Z_{11}^{\perp}}{Z_{22}^{\perp}} = \frac{P_{11}^{\perp}(\theta = 82.4^\circ; \theta_{21})}{P_{22}^{\perp}(\theta = 81.7^\circ; \theta_{21})}, \quad (36)$$

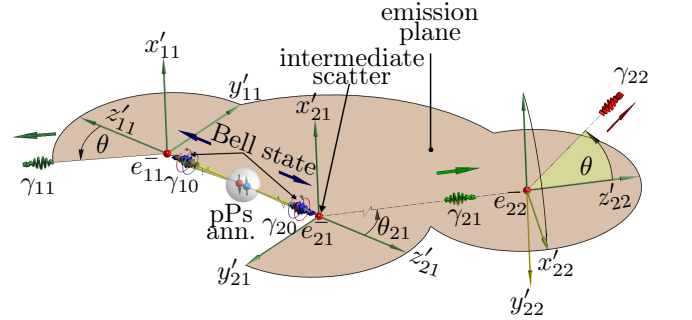
The ratio $Z_{(11,22)}^{\perp}$ is depicted in Fig. 6 as a function of the intermediate scattering angle θ_{21} . The numerator and denominator of this ratio are calculated at the corresponding scattering angles $\theta = 82.4^\circ$ and $\theta = 81.7^\circ$, respectively, where the functions Z_{11}^{\perp} and Z_{22}^{\perp} achieve their maximum value; refer to Fig. 5a and Fig. 5b. In particular, at an intermediate scattering angle of $\theta_{21} = 84.7^\circ$, the frequency of detecting γ_{11} scattering at right angles to the emission plane (Fig. 4b) is expected to be approximately



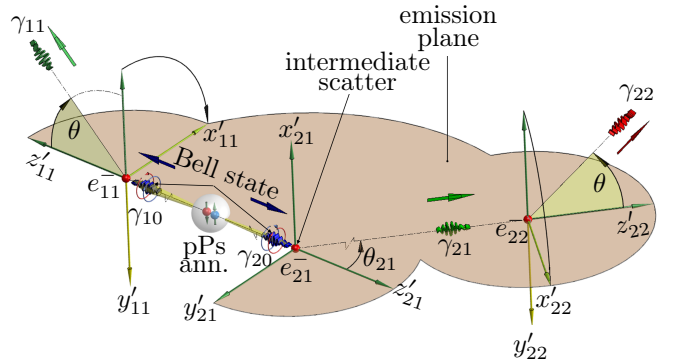
(a) Scattering geometry with γ_{11} and γ_{22} scattering in the emission plane, represented by the probability function $P^{\parallel}(\theta; \theta_{21})$.



(b) Scattering geometry with γ_{11} scattering perpendicular to the emission plane and γ_{22} scattering in the emission plane, described by the probability function $P_{11}^{\perp}(\theta; \theta_{21})$.

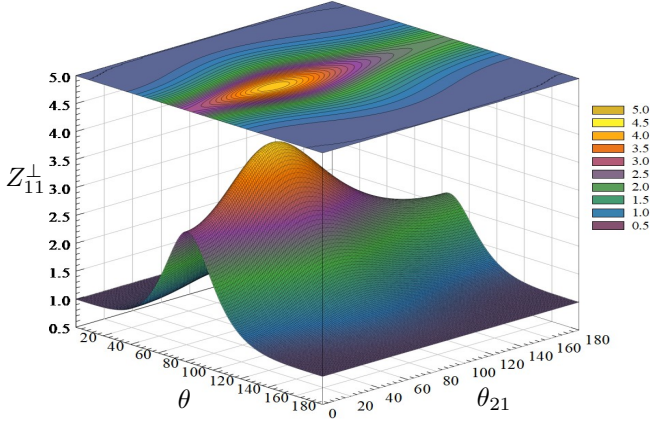


(c) Scattering geometry with γ_{11} scattering in the emission plane and γ_{22} scattering perpendicular to the emission plane, described by the probability function $P_{22}^{\perp}(\theta; \theta_{21})$.

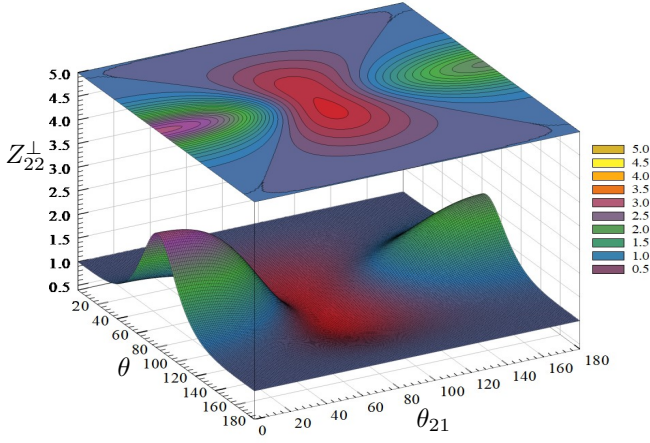


(d) Scattering geometry with γ_{11} and γ_{22} scattering perpendicular to the emission plane, described by the probability function $P_{(11,22)}^{\perp}(\theta; \theta_{21})$.

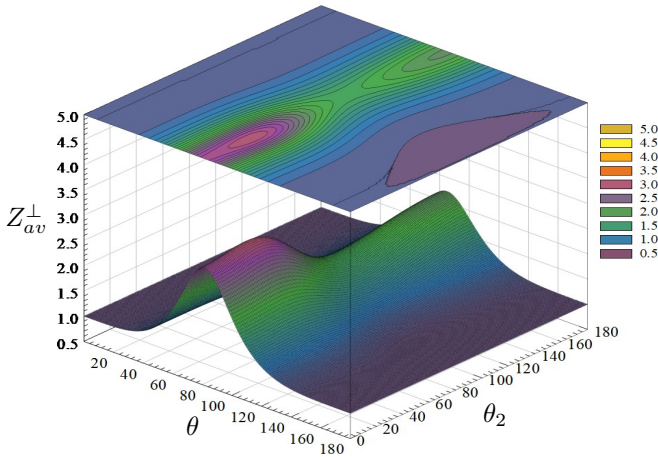
FIG. 4: The four analyzed scattering patterns depict the scattering of γ_{11} and γ_{22} either within or perpendicular to the emission plane.



(a) The counting ratio $Z_{11}^{\perp}(\theta; \theta_{21})$ reaches its maximum value of 4.0 at $(\theta = 82.4^\circ, \theta_{21} = 59.4^\circ)$. It is obtained by dividing the counting rates in Fig. 4b by those in Fig. 4a.



(b) The counting ratio $Z_{22}^{\perp}(\theta; \theta_{21})$ reaches its maximum value of 2.8 at $(\theta = 81.7^\circ, \theta_{21} = 0^\circ)$ and a minimum value of 0.5 at $(\theta = 98.5^\circ, \theta_{21} = 86.6^\circ)$. It is obtained by dividing the counting rates shown in Fig. 4c by those in Fig. 4a.



(c) The average of the counting ratio $Z_{av}^{\perp}(\theta; \theta_{21})$ (Fig. 5a and Fig. 5b) achieves its maximum and minimum values of 3.0 and 1.9 at $(\theta = 82.2^\circ, \theta_{21} = 34.2^\circ)$ and $(\theta = 82.2^\circ, \theta_{21} = 106.2^\circ)$, respectively, refer to Eq.(35b).

FIG. 5: The counting ratios as given in Eq.(35).

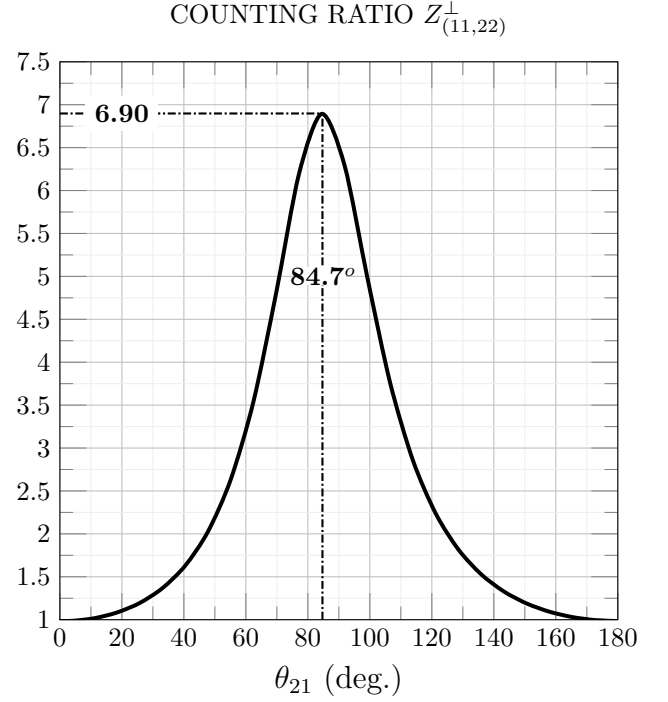


FIG. 6: The counting ratio $Z_{(11,22)}^{\perp} = Z_{11}^{\perp} / Z_{22}^{\perp}$ is obtained by evaluating Z_{11}^{\perp} at $\theta = 82.4^\circ$ (refer to Fig. 5a) and Z_{22}^{\perp} at $\theta = 81.7^\circ$ (refer to Fig. 5b).

seven times greater compared to the scenario where γ_{22} scatters at right angles to the emission plane (Fig. 4c).

We have additionally examined the correlations in the coincidence counting rates of γ_{11} and γ_{22} as a function of the relative angle between the normal of each scattering plane defined by the unit vectors $\hat{\mathbf{x}}'_{11}$ and $\hat{\mathbf{x}}'_{22}$, respectively.

Using Eq.(31), we define an azimuthal correlation function for 3-Compton scattering, denoted as R such that

$$R(\phi_{11}, \phi_{22}; \theta_{11}, \theta_{21}, \theta_{22}) = \frac{P}{A} = \alpha - \beta C, \quad (37a)$$

where

$$\alpha = 1 + \frac{D}{A} \quad \text{and} \quad \beta = \frac{B}{A}. \quad (37b)$$

The dependent variable of R is characterized by the azimuthal angles ϕ_{11} and ϕ_{22} , and parameterized with respect to the Compton scattering angles θ_{11} , θ_{21} and θ_{22} .

In the general case, the scalar product of the normal to each scattering plane can be characterized as

$$\hat{\mathbf{x}}'_{11} \cdot \hat{\mathbf{x}}'_{22} = \cos \phi_{11} \cos \phi_{22} - \cos \theta_{21} \sin \phi_{11} \sin \phi_{22}. \quad (38)$$

We examine these correlations under two distinct scenarios: In the first scenario and referring to Eq.(37a) and

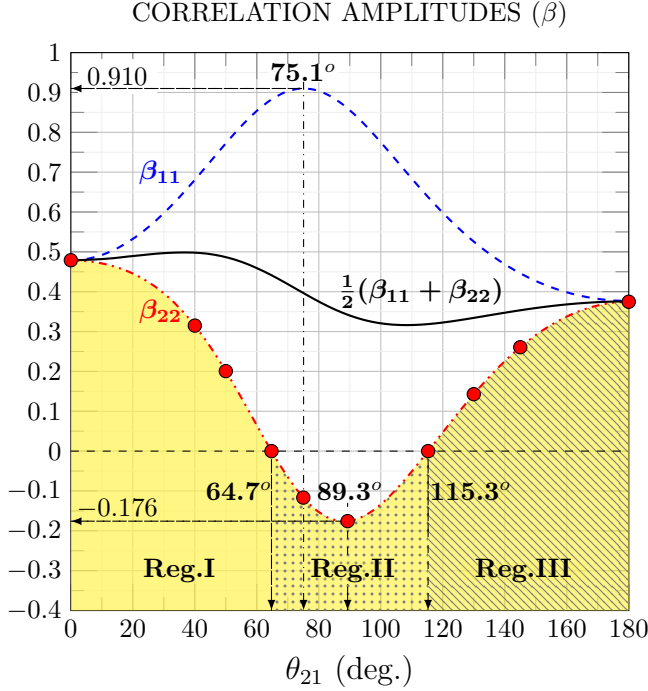


FIG. 7: The correlation amplitudes evaluated for γ_{11} and γ_{22} scattering at specified angles of $\theta_{11} = \theta_{22} = \theta$. In the case of β_{11} ($\theta = 82.4^\circ$) (---). In the case of β_{22} ($\theta = 81.7^\circ$) (-.-.-). These results are shown in conjunction with their average $\frac{1}{2}(\beta_{11} + \beta_{22})$ (—). On the curve $\beta_{22}(\theta = 81.7^\circ)$, the specific points marked by red circles (●) correspond to instances where the behavior of the function $R_{22}(\phi_{22})$ is visually demonstrated in Fig. 8.

Eq.(32c), we set $\phi_{22} = 0$ and find that

$$R_{11}(\phi_{11}; \theta_{11}, \theta_{21}, \theta_{22}) = \alpha_{11} - \beta_{11} \cos 2\phi_{11}. \quad (39)$$

where

$$\alpha_{11}(\theta_{21}, \theta_{22}) = 1 + \frac{t_{12}^{(21)} t_{12}^{(22)}}{t_{11}^{(21)} t_{11}^{(22)}}, \quad (40a)$$

and the corresponding correlation amplitude is given by

$$\beta_{11}(\theta_{11}, \theta_{21}, \theta_{22}) = \frac{t_{12}^{(11)} [2t_{12}^{(22)} + t_{12}^{(21)} (t_{11}^{(22)} - t_{12}^{(22)})]}{t_{11}^{(11)} t_{11}^{(21)} t_{11}^{(22)}}. \quad (40b)$$

Similarly in the second scenario, we set $\phi_{11} = 0$, and find that

$$R_{22}(\phi_{22}; \theta_{11}, \theta_{21}, \theta_{22}) = \alpha_{22} - \beta_{22} \cos 2\phi_{22}. \quad (41)$$

where

$$\alpha_{22}(\theta_{11}, \theta_{21}) = 1 - \frac{t_{12}^{(11)} t_{12}^{(21)}}{t_{11}^{(11)} t_{11}^{(21)}}, \quad (42a)$$

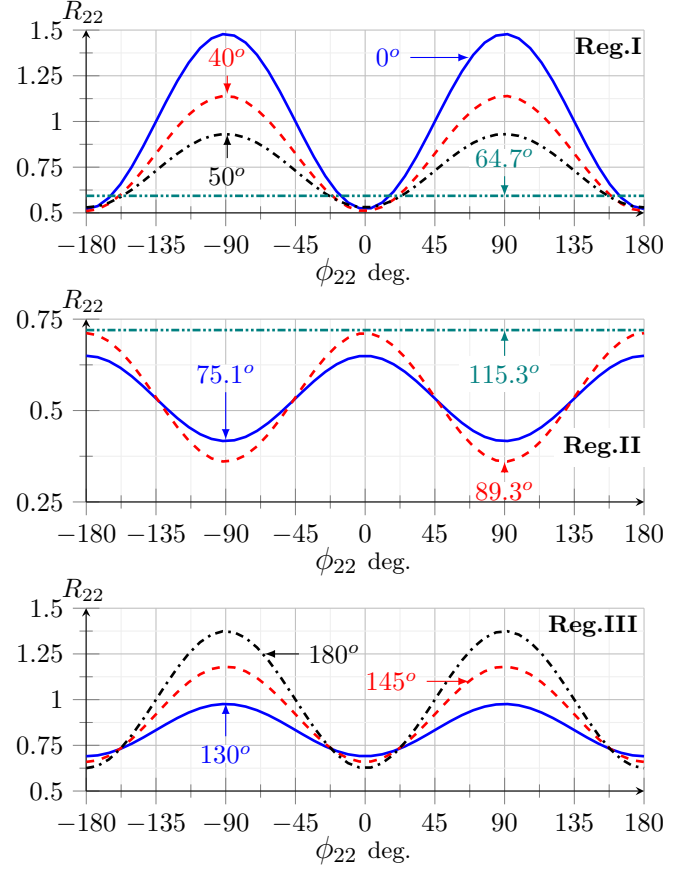


FIG. 8: The function $R_{22}(\phi_{22}; \theta_{21})$ is evaluated for γ_{11} and γ_{22} scattering at a fixed angle of $\theta_{11} = \theta_{22} = \theta = 81.7^\circ$. The plots are calculated for various values of the intermediate scattering angle θ_{21} indicated by solid red circles along the plot of β_{22} plotted in Fig. 7. In particular, a sign change in the correlation amplitude is observed in Region II. Furthermore, no azimuthal correlations are predicted at two specific intermediate angles, namely $\theta_{21} = 64.7^\circ$ and 115.3° . The values of α_{22} and its corresponding correlation amplitude β_{22} for these graphs are provided in the Tab. I.

and the corresponding correlation amplitude is given by

$$\beta_{22}(\theta_{11}, \theta_{21}, \theta_{22}) = \frac{t_{12}^{(22)} [t_{12}^{(11)} (2 - t_{12}^{(21)}) - t_{11}^{(11)} t_{12}^{(21)}]}{t_{11}^{(11)} t_{11}^{(21)} t_{11}^{(22)}}. \quad (42b)$$

In these specific scenarios, the scattering geometry resembles those illustrated in Fig. 4b and Fig. 4c respectively. However, the distinction lies in the fact that in the first scenario (when $\phi_{22} = 0$), the azimuthal angle ϕ_{11} of γ_{11} can assume any value between $-\pi \leq \phi_{11} \leq \pi$. Similarly, in the second scenario (when $\phi_{11} = 0$), the azimuthal angle ϕ_{22} of γ_{22} is also unrestricted and can vary between $-\pi \leq \phi_{22} \leq \pi$. In these two particular scattering scenarios, the angle ϕ_{11} or ϕ_{22} serves as a direct indicator of the relative angle between the scattering planes,

TABLE I: In the context of an ideal experiment, the numerical values are provided for α_{22} and their associated correlation amplitudes β_{22} . These theoretical values correspond to specific instances where the behavior of the function R_{22} is visually demonstrated in Fig. 8.

$R_{22}(\phi_{22}; \theta_{21}, \theta = 81.7^\circ) = \alpha_{22} - \beta_{22} \cos 2\phi_{22}$						
	Region I		Region II		Region III	
θ_{21} (deg.)	α_{22}	β_{22}	α_{22}	β_{22}	α_{22}	β_{22}
0	1.000	+0.479				
40	0.825	+0.315				
50	0.731	+0.201				
64.734	0.593	0				
75			0.533	-0.117		
89.291			0.536	-0.176		
115.266			0.720	0		
130					0.833	+0.143
145					0.920	+0.261
180					1.000	+0.375

since in the first scenario we have $\hat{\mathbf{x}}'_{11} \cdot \hat{\mathbf{x}}'_{22} = \cos \phi_{11}$ and in the second we have $\hat{\mathbf{x}}'_{11} \cdot \hat{\mathbf{x}}'_{22} = \cos \phi_{22}$ (cf. evaluating Eq.(38)).

The plots of correlation amplitudes β_{11} and β_{22} , along with their average $\frac{1}{2}(\beta_{11} + \beta_{22})$, as functions of the intermediate scattering angle θ_{21} are shown in Fig. 7. These plots correspond to the scenario in which the scattering angles θ_{11} and θ_{22} are set to θ . Specifically, β_{11} is evaluated at $\theta = 82.4^\circ$, while β_{22} is evaluated at $\theta = 81.7^\circ$.

An observation can be made in Fig. 7 about the behavior of β_{11} and β_{22} as the intermediate scattering angle θ_{21} increases from zero degrees. Initially, these correlation amplitudes diverge. However, they eventually converge, although at a lower value compared to $\theta_{21} = 0^\circ$ (see Table I for tabulated values). This convergence phenomenon is notable because it occurs when γ_{11} and γ_{22} experience a backscatter at $\theta_{21} = 180^\circ$. Furthermore, it should be noted that initially β_{11} increases monotonically as the intermediate scattering angle increases. It reaches a maximum value of 0.910 around $\theta_{21} = 75.1^\circ$ before monotonically decreasing. In particular, the sign of β_{11} remains positive throughout.

The correlation amplitude β_{22} exhibits varying properties in different regions of the intermediate scattering angle θ_{21} . In Region I ($0 \leq \theta_{21} < 64.7^\circ$), β_{22} maintains a positive sign. However, in Region II ($64.7^\circ < \theta_{21} < 115.3^\circ$), β_{22} changes sign and becomes negative, and in Region III ($115.3^\circ < \theta_{21} \leq 180^\circ$), β_{22} reverts to a positive sign, indicating a return to a scattering behavior similar to that in Region I.

Furthermore, β_{22} reaches a minimum value of -0.176 at $\theta_{21} = 89.3^\circ$ in Region II. Above 89.3° degrees, β_{22} begins to increase. At approximately $\theta_{21} = 64.7^\circ$ and

$\theta_{21} = 115.3^\circ$, the correlation amplitude becomes zero, indicating the absence of azimuthal correlations between γ_{11} and γ_{22} .

Figure 8 shows the behavior of R_{22} (Eq. (41)) as a function of the relative angle between the scattering planes, defined by ϕ_{22} , given in degrees, for selected values of θ_{21} highlighted as large solid red circles shown in Fig. 7. Furthermore, the associated values of α_{22} and β_{22} of R_{22} can be found in Table I.

V. CONCLUSION

We use a novel matrix framework to determine for the first time the 3-Compton scattering cross section for entangled annihilation photons. Studies of the predicted azimuthal correlations in different kinematic regions for the scattered photons show large variations, indicating regions where future experimental studies of 3-Compton could be focused to test the fundamental aspects of the theory.

As the 3-Compton process is the leading quantum decoherence mechanism for entangled annihilation photons, this new work will enable a detailed theoretical understanding of the fundamental decoherence process for entangled photons at the MeV scale. Such processes are crucial for accurate modeling of the annihilation photons used in PET, event topology for correlated detection of entangled quanta, and for more accurate fundamental tests at the MeV scale.

The versatility of the current framework allows for easy implementation in Monte Carlo particle simulations. Additionally, it is adaptable, enabling the inclusion of other interaction processes and serving as a foundation for investigating entanglement and decoherence at energy scales that are currently unexplored, such as the GeV energy scale.

ACKNOWLEDGMENTS

The authors gratefully acknowledge the support of the UK Science and Technologies Funding Council (STFC) grant number ST/W006383/1.

Appendix A: Compton transition matrices

The Compton transition matrix T_{pj} is given by

$$T_{pj} = \frac{r_0^2}{2} \left(\frac{E_{pj}}{E_{p(j-1)}} \right)^2 \begin{bmatrix} t_{11}^{(pj)} & t_{12}^{(pj)} & 0 & t_{14}^{(pj)} \\ t_{12}^{(pj)} & 2 - t_{12}^{(pj)} & 0 & t_{24}^{(pj)} \\ 0 & 0 & t_{33}^{(pj)} & t_{34}^{(pj)} \\ t_{41}^{(pj)} & t_{42}^{(pj)} & t_{43}^{(pj)} & t_{44}^{(pj)} \end{bmatrix}, \quad (\text{A1})$$

where $1 \leq j \leq \eta$ and η denotes the total number of Compton scattering events and r_0 represents the classical electron radius. The subscript $p = 1$ or $p = 2$ labels the photon within the 2-photon system. The functional form of the $t_{mn}^{(pj)}$ matrix elements are given in Table II, with further information available in [27, 28].

$E_{p(j-1)}$ defines the kinetic energy of $\gamma_{p(j-1)}$ after the $(j-1)$ -th scattering event and E_{pj} defines the kinetic energy of γ_{pj} after the j -th scattering event, traveling in a direction defined by the angles (ϕ_{pj}, θ_{pj}) . We work in units where $\hbar, c = 1$ and measure the kinetic energies of the photons in units of $mc^2 = 0.511$ MeV.

When $j = 1$, which implies $j - 1 = 0$, then E_{p0} represents the incident energy of γ_{p0} . Otherwise, for $j > 0$, E_{pj} and $E_{p(j-1)}$ are described by the Compton relation formula given by

$$E_{pj} = \frac{E_{p(j-1)}}{1 + E_{p(j-1)}(1 - \cos \theta_{pj})} \quad (1 < j \leq \eta), \quad (\text{A2})$$

where $0 \leq \theta_{pj} \leq \pi$.

Stokes parameters depend on the choice of axes, and a rotation matrix M_{pj} relates the Stokes parameters in one coordinate system to another. If we consider a second coordinate system rotated about the direction of photon propagation at an angle of $2\phi_{pj}$ to the right of the original, the relation is given by [28] such that

$$M_{pj} = \begin{bmatrix} 1 & 0 & 0 & 0 \\ 0 & \cos 2\phi_{pj} & \sin 2\phi_{pj} & 0 \\ 0 & -\sin 2\phi_{pj} & \cos 2\phi_{pj} & 0 \\ 0 & 0 & 0 & 1 \end{bmatrix}, \quad (\text{A3})$$

where $-\pi \leq \phi_{pj} \leq \pi$. (Note that when considering unpolarized electrons, it is sufficient to use only the upper-left 3×3 submatrices given in Eq.(A1) and Eq.(A3).)

Appendix B: Stokes vectors for polarization filters

Stokes parameters for polarization filters, which assess two orthogonal polarization states, are defined in this method with respect to the scattering plane containing the momentum vectors $(\vec{k}_{\eta-1}, \vec{k}_\eta)$, as illustrated in Fig.1. The fundamental pairs of orthogonal filters are the linear, diagonal, and circular polarization filters.

In the case of linear polarization filters, one can analyze the state of polarization orthogonal to the scattering plane with $|D_\perp\rangle$ and parallel to it with $|D_\parallel\rangle$ where

$$|D_\perp\rangle = \begin{bmatrix} 1 \\ 1 \\ 0 \\ 0 \end{bmatrix}, \quad |D_\parallel\rangle = \begin{bmatrix} 1 \\ -1 \\ 0 \\ 0 \end{bmatrix}. \quad (\text{B1})$$

Another set of polarization filters includes the diagonal $|D_{+45}\rangle$ and anti-diagonal $|D_{-45}\rangle$ polarization filters,

which have the explicit form

$$|D_{+45}\rangle = \begin{bmatrix} 1 \\ 0 \\ 1 \\ 0 \end{bmatrix}, \quad |D_{-45}\rangle = \begin{bmatrix} 1 \\ 0 \\ -1 \\ 0 \end{bmatrix}. \quad (\text{B2})$$

The final pair of polarization filters includes the right circular $|D_r\rangle$ and left circular $|D_l\rangle$ polarization filters, given by

$$|D_r\rangle = \begin{bmatrix} 1 \\ 0 \\ 0 \\ -1 \end{bmatrix}, \quad |D_l\rangle = \begin{bmatrix} 1 \\ 0 \\ 0 \\ 1 \end{bmatrix}. \quad (\text{B3})$$

Using a polarization-insensitive detector implies making an average measurement of two orthogonal states and summing the results. Let $|I\rangle$ represent a polarization-insensitive detector. In the context of the fundamental pairs of orthogonal filters we have

$$\begin{aligned} |I\rangle &= \frac{1}{2} |D_\perp\rangle + \frac{1}{2} |D_\parallel\rangle, \\ |I\rangle &= \frac{1}{2} |D_{+45}\rangle + \frac{1}{2} |D_{-45}\rangle, \\ |I\rangle &= \frac{1}{2} |D_r\rangle + \frac{1}{2} |D_l\rangle, \end{aligned} \quad (\text{B4})$$

$$|I\rangle = \begin{bmatrix} 1 \\ 0 \\ 0 \\ 0 \end{bmatrix}.$$

Appendix C: Matrix element definitions for 3-Compton scattering

The Compton transition matrix elements relevant to the 3-Compton cross section have the following functional forms:

For $\gamma_{10} \mapsto \gamma_{11}$

$$t_{11}^{(11)} = 1 + \cos^2 \theta_{11} + (E_{10} - E_{11})(1 - \cos \theta_{11}), \quad (\text{C1a})$$

$$t_{12}^{(11)} = \sin^2 \theta_{11}, \quad (\text{C1b})$$

where $E_{10} = 1$ and

$$E_{11} = \frac{1}{2 - \cos \theta_{11}}; \quad (\text{cf. Eq.(23)}). \quad (\text{C2})$$

For $\gamma_{20} \mapsto \gamma_{21}$

$$t_{11}^{(21)} = 1 + \cos^2 \theta_{21} + (E_{20} - E_{21})(1 - \cos \theta_{21}), \quad (\text{C3a})$$

TABLE II: Definitions of the matrix elements $t_{mn}^{(pj)}$, where $1 \leq j \leq \eta$ and η is the total number of Compton scattering events and $p = 1, 2$ denote photon 1 or 2. Unit momentum vectors $\hat{\mathbf{k}}_{p(j-1)}$ and $\hat{\mathbf{k}}_{pj}$ define the direction of incident and scatter of γ_{p0} in its interaction with the j -th electron (refer to Fig.1). The unit vector $\hat{\mathbf{S}}_{pj} = (x_{pj}, y_{pj}, z_{pj})$, where $x_{pj}^2 + y_{pj}^2 + z_{pj}^2 = 1$, defines the spin direction of the j -th incident electron.

(a) Spin independent terms	(b) Spin dependent terms
$t_{11}^{(pj)} = 1 + \cos^2 \theta_{pj} + (E_{p(j-1)} - E_{pj}) (1 - \cos \theta_{pj})$	$t_{14}^{(pj)} = -(1 - \cos \theta_{pj}) (E_{p(j-1)} \cos \theta_{\hat{\mathbf{k}}_{p(j-1)}} + E_{pj} \hat{\mathbf{k}}_{pj}) \cdot \hat{\mathbf{S}}_{pj}$
$t_{12}^{(pj)} = t_{21}^{(pj)} = \sin^2 \theta_{pj}$	$t_{24}^{(pj)} = E_{p(j-1)} (1 - \cos \theta_{pj}) (\hat{\mathbf{k}}_{pj} \times \hat{\mathbf{k}}_{p(j-1)}) \cdot (\hat{\mathbf{k}}_{p(j-1)} \times \hat{\mathbf{S}}_{pj})$
$t_{13}^{(pj)} = t_{23}^{(pj)} = t_{31}^{(pj)} = t_{32}^{(pj)} = 0$	$t_{34}^{(pj)} = E_{p(j-1)} (1 - \cos \theta_{pj}) (\hat{\mathbf{k}}_{p(j-1)} \times \hat{\mathbf{k}}_{pj}) \cdot \hat{\mathbf{S}}_{pj}$
$t_{22}^{(pj)} = 2 - t_{12}^{(pj)} = 2 - \sin^2 \theta_{pj}$	$t_{41}^{(pj)} = -(1 - \cos \theta_{pj}) (E_{pj} \cos \theta_{\hat{\mathbf{k}}_{pj}} + E_{p(j-1)} \hat{\mathbf{k}}_{p(j-1)}) \cdot \hat{\mathbf{S}}_{pj}$
$t_{33}^{(pj)} = 2 \cos \theta_{pj}$	$t_{42}^{(pj)} = E_{pj} (1 - \cos \theta_{pj}) (\hat{\mathbf{k}}_{p(j-1)} \times \hat{\mathbf{k}}_{pj}) \cdot (\hat{\mathbf{k}}_{pj} \times \hat{\mathbf{S}}_{pj})$
$t_{44}^{(pj)} = 2 \cos \theta_{pj} + (E_{p(j-1)} - E_{pj}) (1 - \cos \theta_{pj}) \cos \theta_{pj}$	$t_{43}^{(pj)} = -E_{pj} (1 - \cos \theta_{pj}) (\hat{\mathbf{k}}_{p(j-1)} \times \hat{\mathbf{k}}_{pj}) \cdot \hat{\mathbf{S}}_{pj}$

$$t_{12}^{(21)} = \sin^2 \theta_{21}, \quad (\text{C3b})$$

$$t_{12}^{(22)} = \sin^2 \theta_{22}, \quad (\text{C5b})$$

where

$$t_{33}^{(21)} = 2 \cos \theta_{21}, \quad (\text{C3c})$$

$$E_{22} = \frac{E_{21}}{1 + E_{21} (1 - \cos \theta_{22})}; \quad (\text{cf. Eq.(27b)}). \quad (\text{C6})$$

where $E_{20} = 1$ and

$$E_{21} = \frac{1}{2 - \cos \theta_{21}}; \quad (\text{cf. Eq.(27a)}). \quad (\text{C4})$$

For $\gamma_{21} \mapsto \gamma_{22}$

$$t_{11}^{(22)} = 1 + \cos^2 \theta_{22} + (E_{21} - E_{22}) (1 - \cos \theta_{22}), \quad (\text{C5a})$$

-
- [1] A. W. Chin, S. F. Huelga, and M. B. Plenio, *Phys. Rev. Lett.* **109**, 233601 (2012).
- [2] M. Foss-Feig, K. R. A. Hazzard, J. J. Bollinger, and A. M. Rey, *Phys. Rev. A* **87**, 042101 (2013).
- [3] M. H. L. Pryce and J. C. Ward, *Nature* **160**, 435 (1947).
- [4] H. S. Snyder, S. Pasternack, and J. Hornbostel, *American Physical Society* **73**, 440 (1948).
- [5] D. Bohm and Y. Aharonov, *Phys. Rev.* **108**, 1070 (1957).
- [6] V. D. Irby, *Phys. Rev. A* **67**, 034102 (2003).
- [7] I. Gauthier and M. Hawton, *Phys. Rev. A* **81**, 062121 (2010).
- [8] G. J. Roizing, P. E. Mijnders, and R. Benedek, *Phys. Rev. B* **43**, 6996 (1991).
- [9] S. D. Bass, S. Mariazzi, P. Moskal, and E. Stępień, *Rev. Mod. Phys.* **95**, 021002 (2023).
- [10] S. Basu, T. C. Kwee, S. Surti, E. A. Akin, D. Yoo, and A. Alavi, *Annals of the New York Academy of Sciences* **1228**, 1 (2011).
- [11] E. Nevo, P. Kamvosoulis, and G. Currie, *Journal of Nuclear Medicine Technology* **50**, 17 (2022).
- [12] J. M. Ollinger, *Physics in Medicine & Biology* **41**, 153 (1996).
- [13] J. S. Barney, J. G. Rogers, R. Harrop, and H. Hoverath, *IEEE Transactions on Nuclear Science* **38**, 719 (1991).
- [14] A. Zatcepin and S. I. Ziegler, *Zeitschrift für Medizinische Physik* **33**, 4 (2023), special Issue: Recent Developments in Nuclear Medicine Imaging and Therapy.
- [15] C. S. Levin, *Proceedings of the IEEE* **96**, 439 (2008).
- [16] H. Zaidi, M. L. Montandon, and S. Meikle, *NeuroImage* **34**, 518 (2007).
- [17] A. Koide, J. Kataoka, T. Masuda, S. Mochizuki, T. Taya, K. Sueoka, L. Tagawa, K. Fujieda, T. Maruhashi, T. Kurihara, and T. Inaniwa, *Scientific Reports* **8**, 8116 (2018).
- [18] L. R. Kasday, J. D. Ullman, and C. S. Wu, *Il Nuovo Cimento B (1971-1996)* **25**, 633 (1975).
- [19] D. P. Watts, J. Bordes, J. R. Brown, A. Cherlin, R. Newton, J. Allison, M. Bashkanov, N. Efthimiou, and N. A. Zachariou, *Nature Communications* **12** (2021).
- [20] M. Uenomachi, M. Takahashi, K. Shimazoe, H. Takahashi, K. Kamada, T. Orita, K. Ogane, and A. B. Tsuji, *Scientific Reports* **11**, 17933 (2021).
- [21] B. C. Hiesmayr and P. Moskal, *Sci Rep* **9**, 8166 (2019).
- [22] A. L. McNamara, M. Toghyani, J. E. Gillam, K. Wu, and Z. Kuncic, *Physics in Medicine and Biology* **59**, 7587 (2014).
- [23] A. Strizhak, D. Abdurashitov, A. Baranov, A. Ivashkin, and S. Musin, *Physics of Particles and Nuclei Letters* **19**, 509 (2022).
- [24] A. Ivashkin, D. Abdurashitov, A. Baranov, F. Guber,

- S. Morozov, S. Musin, A. Strizhak, and I. Tkachev, *Scientific Reports* **13**, 7559 (2023).
- [25] P. Moskal, D. Kisielewska, C. Curceanu, E. Czerwiński, K. Dulski, A. Gajos, M. Gorgol, B. Hiesmayr, B. Jasińska, K. Kacprzak, L. Kapłon, G. Korcyl, P. Kowalski, W. Krzemień, T. Kozik, E. Kubicz, M. Mohammed, S. Niedźwiecki, M. Pałka, M. Pawlik-Niedźwiecka, L. Raczyński, J. Raj, S. Sharma, Shivani, R. Y. Shopa, M. Silarski, M. Skurzok, E. Stepień, W. Wiślicki, and B. Zgardzińska, *Physics in Medicine & Biology* **64**, 055017 (2019).
- [26] A. Wightman, *Phys. Rev.* **74**, 1813 (1948).
- [27] U. Fano, *J. Opt. Soc. Am.* **39**, 859 (1949).
- [28] W. H. McMaster, *Reviews of Modern Physics* **33**, 8 (1961).
- [29] Y. Taira, S. Endo, S. Kawamura, T. Nambu, M. Okuizumi, T. Shizuma, M. Omer, H. Zen, Y. Okano, and M. Kitaguchi, *Phys. Rev. A* **107**, 063503 (2023).
- [30] F. Wan, Y. Wang, R.-T. Guo, Y.-Y. Chen, R. Shaisultanov, Z.-F. Xu, K. Z. Hatsagortsyan, C. H. Keitel, and J.-X. Li, *Phys. Rev. Res.* **2**, 032049(R) (2020).
- [31] S. Stock, A. Surzhykov, S. Fritzsche, and D. Seipt, *Phys. Rev. A* **92**, 013401 (2015).
- [32] N. Danneberg, W. Fetscher, K.-U. Köhler, J. Lang, T. Schweizer, A. von Allmen, K. Bodek, L. Jarczyk, S. Kistryn, J. Smyrski, A. Strzałkowski, J. Zejma, K. Kirch, A. Kozela, and E. Stephan, *Phys. Rev. Lett.* **94**, 021802 (2005).
- [33] G. Schmidt and L. M. Simons, *Z. Physik* **263**, 387 (1973).
- [34] The binding energy of the electron for light atomic nuclei is around 1% of the kinetic energy of the annihilation photon and reaches 4% for heavier nuclei [35]. These effects are accounted for in simulation, i.e. the electron energy is reduced according to the average binding energy of the atom involved in the Compton scattering. Compton scattering is calculated in the frame where the electron is stationary and then boosted into the laboratory frame to account for the Fermi motion.
- [35] M. A. Zoroddu, J. Aaseth, G. Crisponi, S. Medici, M. Peana, and V. M. Nurchi, *Journal of Inorganic Biochemistry* **195**, 120 (2019).